Approaching Theoretical Band Gap of ZnSnN 2 Films via Bias Magnetron Cosputtering at Room Temperature

Agathe Virfeu, Fahad Alnjiman, Jaafar Ghanbaja, Alejandro Borroto, Christine Gendarme, Sylvie Migot, Leonardo Kopprio, Sylvain Le Gall, Christophe Longeaud, Jean-Pierre Vilcot, et al.

Approaching theoretical band gap of ZnSnN2 films via bias magnetron co-sputtering at room temperature

Agathe Virfeu,[†] Fahad Alnjiman,[†, §] Jaafar Ghanbaja,[†] Alejandro Borroto,[†] Christine Gendarme,[†] Sylvie Migot,[†] Leonardo Koppio,[‡] Sylvain Le Gall,[‡] Christophe Longeaud,[‡] Jean-Pierre Vilcot,[‖] Jean-François Pierson[*,†]

[†]Institut Jean Lamour, UMR 7198, CNRS, Université de Lorraine, 2 allée André Guinier, Campus ARTEM, B.P. 50840, 54011 Nancy Cedex, France

[§]Department of Physics and Astronomy at College of Science, King Saud University at Riyadh, Saudi Arabia

[‡]Laboratoire de Génie Electrique et Electronique de Paris (Geeps), CNRS, CentraleSupelec, Université Paris Saclay, Sorbonne Université, 11 rue Joliot Curie, 91190, Gif sur Yvette, France

[‖] Univ. Lille, CNRS, Centrale Lille, Univ. Polytechnique Hauts-de-France, UMR 8520 - IEMN - Institut d'Electronique de Microélectronique et de Nanotechnologie, F-59000 Lille, France

ABSTRACT: Zinc tin nitride ($ZnSnN_2$) is a promising semiconductor candidate for solar cell applications and optoelectronic devices. However, the practical use of this material has been limited by several issues as, among others, oxygen contamination, a very high concentration of free carriers and the difficulty to reach the theoretically predicted band gap. Here, we deposit thin films of $ZnSnN_2$ by reactive DC magnetron cosputtering at room temperature with an RF bias power (P_b) in the range 0-50 W. Using first principle calculations, we explore the structural and opto-electronic properties that are favorably compared to experimental results. We demonstrate that the optical band gap energy can be decreased from 1.7 eV to 1.34 eV, close to the predicted value of 1.37 eV. The free electron concentration is decreased down to 10^{17} cm^{-3} which results in the reduction of the absorption by free electrons in the IR range. In addition, in a given range of applied bias powers, we observe a densification of the films and significant decrease of their oxygen contamination from 6.7 down to 2.0 at. % . The study underlines that a value of 20 W power bias leads to the optimal structural, optical and electrical properties. Our results provide an interesting method to obtain a potential candidate for photovoltaic application, in an environmental friendly way, for a low-cost industrialization.

INTRODUCTION

Since the dawn of the 21st century, the constant research of new renewable energy sources has become a global challenge. To overcome the massive exploitation of polluting fossil fuels and the energy needs of the world's growing population, the solar energy conversion requires new materials to design photovoltaic cells and improve their efficiency. $ZnSnN_2$ (ZTN) is an alternative to the III-V compounds composed of Ga and In, which became expensive due to the depletion of the mining resources[1]. Zn-IV-N_2 is a potential candidate's family of compounds constituted by earth-abundant and nontoxic elements. Some groups have already investigated the use of $ZnSnN_2$ as an absorbent layer in solar cells.[2-4]

$ZnSnN_2$ provides a tunable band gap energy and a high absorption coefficient.[5, 6] The Zn-IV-N_2 type compounds would cover a large part of the solar spectrum for bandgap energies ranging from 1.4 eV ($ZnSnN_2$) to 5.7 eV ($ZnSiN_2$).[7] The structure of these compounds is closely related to the III-N semiconductor ones with III= Al, Ga, In, which are thermodynamically stable, and where the element of column III is replaced by a sublattice of zinc and atoms of column IV (Si, Ge, Sn).[8] The structure of this family of semiconductors is not well defined; the most stable one is orthorhombic with 16 atoms per unit cell: 4 atoms of zinc, 4 atoms of column IV elements and 8 atoms of nitrogen. The space group of this structure is $Pna2_1$ corresponding to the β-$NaFeO_2$-type. The other possible structure is the wurtzite-like known from the (Al, Ga, In)-N family structure with a hexagonal space group lattice $P6_3mc$. The difference between these two structures is the organization of the cation sublattice: the orthorhombic structure is ordered while the wurtzite one is disordered because the Zn and the atoms of column IV are randomly positioned.[9, 10]

The first work concerning the growth of $ZnSnN_2$ thin films by plasma-assisted molecular beam epitaxy (PAMBE) was published in 2011.[11] Since this article, the number of papers has continued to increase in both theoretical[12-16] and experimental approaches; scientists attempt to understand structure-properties relationships in order to discover a class of materials that can compete with the actual photovoltaic absorbers market leaders.[17] Synthesis techniques progressed significantly, from plasma-assisted vapor–liquid–solid technique,[18] RF and DC magnetron sputtering,[19, 20] metathesis reaction under high pressure,[21] combinatorial reactive sputtering using $Zn-Sn_3N_4$ alternative layers,[22] to PAMBE with ZnO buffer on Al_2O_3 substrate.[23] However, the optoelectronic properties of these materials are still challenging and not really mastered due to the huge disparity between the results of the various studies. Many theoretical studies have been carried out to help the understanding of experimental observations. In 2013, Lahourcade *et al.* proposed an approximation of the band gap energy value of E_G = 1.42 eV for an orthorhombic $ZnSnN_2$ structure with a hybrid functional (HSE06), which is, nowadays, one of the most accurate.[19]

One of the main challenges in the study of $ZnSnN_2$ is the difficulty to reach low carrier concentration because of the low formation energy of the donor-like intrinsic defects. Most of the time, high n-type carrier concentration in the range of $10^{19}-10^{21}$ cm^{-3} are obtained.[19, 24, 43] Postannealing treatments have been demonstrated to be a viable route for lowering the carrier concentration (in the range of $10^{17}-10^{18}$ cm^{-3}) in stoichiometric films.[27, 35] Another route is the deposition of films

with over stoichiometry in zinc to suppress the Zn_{Sn} defect. In this way, a carrier concentration of approximately 4×10^{16} cm^{-3} has been reported for $Zn_{1.36}Sn_{0.64}N_2$ thin films.[44] A good mastering of carrier concentration in the range of 10^{16}– 10^{19} cm^{-3} was reported for amorphous and microcrystalline ZTN films obtained by RF magnetron sputtering.[45]

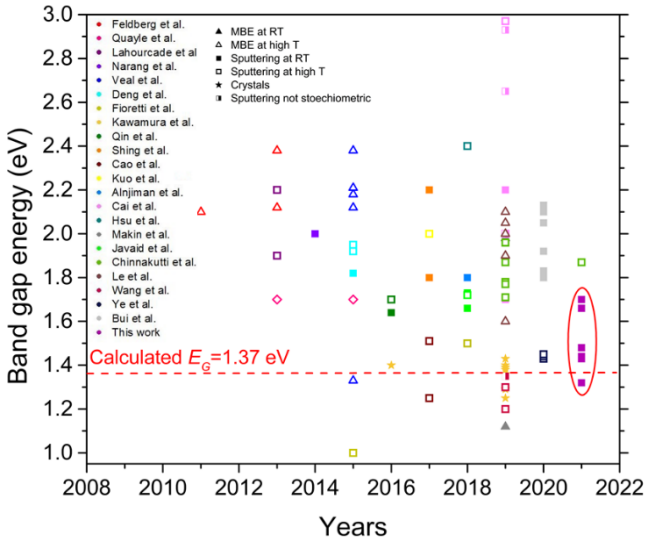

Figure 1. Comparison of experimental band gap energy obtained in the literature (colors) for $ZnSnN_2$, using different methods of synthesis at different deposition temperatures (symbols), with the calculated band gap energy and the experimental optical band gap energy of this work[2, 4, 5, 7, 9, 11, 18-22, 24-42]

So far, few works have investigated oxygen contamination in $ZnSnN_2$ thin films. A previous experimental work, accomplished in our group, highlighted the content of oxygen at the column boundaries, by EDS measurements in STEM mode and Mössbauer experiments.[29] A theoretical work studied the disorder caused by unintentional oxygen incorporation, by considering the additional effects of nonequilibrium synthesis, off-stoichiometry and disorder.[46] In $ZnSnN_2$, atomic substitution is possible also on cation Zn_{Sn} and anion O_N sublattices.[47] In other nitrides such as InN, high free carrier densities due to unintentional oxygen incorporation led to degenerate carrier doping and an overestimation of the bandgap by more than 1 eV due to the Burstein–Moss shift.[48] It appeared that the unusual doping did not depend on O content, but resulted from the composition, which induced changes in the electronic structure. To reduce oxygen contamination and to improve physico-chemical properties, a new approach was investigated by the use of bias during film growth.[30] It is well-known that the film properties are governed by the processing parameters as pressure, temperature, and bias voltage among others. A negative bias voltage applied to the substrate can significantly improve the ionization and energy of the sputtered particles and enhance the film crystallization by increasing the grain size.[49]

Moreover, by reviewing the optical band gap energy obtained during ten years in the literature (Fig. 1), we noticed that most of the groups have used temperature-dependent parameters. To find a low-cost industrialization process, we decided to change the way of working by using room temperature sputtering with bias during the growth of the films.

In this study, we report the use of a negative bias applied to the substrate holder, ranging from 0 to 50 W, during reactive co-sputtering of $ZnSnN_2$ films. The resulting modifications of the film morphology, the texture, the oxygen content and distribution as well as the optical and electronic properties will be presented and detailed.

EXPERIMENTAL SECTION

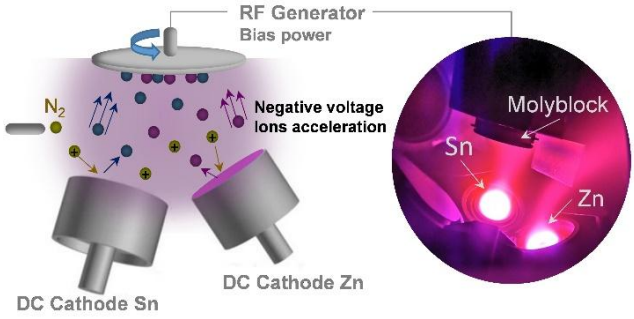

Figure 2. Representation of the reactive bias magnetron co-sputtering apparatus and an image of the actual deposition chamber during a growth of ZTN.

A schematic representation of the reactive magnetron co-sputtering apparatus used in this work is illustrated in Fig. 2, which is an equipment composed of four targets in confocal position relative to the substrate. ZTN films were deposited by direct current (DC) magnetron co-sputtering on intrinsic Si (100)-oriented wafer and soda-lime glass substrates. Two metallic targets (2.00" diameter and 0.125" thick) of tin and zinc (purity higher than 99.9%) were used as sputtering sources, in pure reactive nitrogen gas, without external heating. The deposition system was arranged with a load lock chamber to facilitate substrates exchange. The substrates were cleaned with ethanol and dried with compressed air gun before their introduction into the deposition chamber. Via mechanical and turbo-molecular pumps, the base pressure in the chamber was systematically lower than 10^{-7} mbar. Preceding the deposition, the substrates were cleaned *in situ* by radiofrequency (RF) sputter etching (50 W during 10 min) using a mixture of Ar/N_2 (1/3). The addition of argon in the gas mixture for the target cleaning allowed for improving the efficiency of this step. The target to substrate distance was fixed at 9 cm (the smallest distance available). Constant currents of 0.10 A and 0.25 A were applied to the zinc and tin targets, respectively. A presputter step of 2 min with the same current targets was performed. The nitrogen flow rate was adjusted to 30 sccm and a working nitrogen pressure of 1 Pa was used. The total pressure was measured using a Baratron gauge.

A RF (13.56 MHz) bias power (P_b) between 0 and 50 W was applied to the substrate holder during the deposition step. To ensure chemical homogeneity of the films, the substrate holder was rotating (10 rpm). ZTN films were deposited without intentional heating. The self-established temperature at the substrate was measured using a thermocouple and did not exceed 80 °C during growth. The deposition duration was fixed at 30 min leading to a thickness higher than 1 µm.

The structure of the samples was studied by X-ray diffraction (XRD) measurements in the Bragg-Brentano configuration with Cu Kα radiation (λ = 0.15406 nm) using an AXS Bruker D8 Advance diffractometer. To characterize the film morphology, top and cross-sectional scanning electron micrographs were taken using a Zeiss Gemini 500 scanning electron microscope (SEM). The film thicknesses were also measured

on the cross-sectional micrographs. The obtained values were in agreement with thickness measurement using a stylus profilometer. Transmission electron microscopy (TEM) investigations were carried out using a JEM - ARM 200F Cold FEG TEM/STEM operating at 200 kV and equipped with a spherical aberration (Cs) probe and image correctors (point resolution 0.12 nm in TEM mode and 0.078 nm in STEM mode). The cross-section of the samples was prepared by using a focused ion beam (FIB) scanning electron microscope (SEM) dual beam system FEI Helios NanoLab 600i. The surface topography of the films and root mean square (RMS) roughness (R_q) were examined in resonant mode using a Nano-Observer Atomic Force Microscope developed by CSInstruments.

The chemical composition of the samples was determined by wavelength dispersive X-ray spectroscopy (WDS) using a JEOL JXA-8530F instrument. Zn, Sn, Fe_4N and MgO were used as standards to measure the Zn, Sn, N and O concentrations, respectively. For each sample, the reported chemical compositions were obtained by averaging 100 different spots measured on the surface (~ 200×200 µm²). This method is more accurate to determine the concentration of light elements as nitrogen and oxygen.

The optical UV-visible absorption measurements were performed in the 200-2500 nm range using Varian Cary 7000 UV-Vis-NIR spectrometer with in an UMA configuration. A correction for substrate reflection has been done to determine the band gap energy by Tauc plot method.[50-54] The total measured transmittance is given by T_{exp}. To suppress the influence of the substrate (T_{subs}), we corrected the film transmittance with *eq. (1)*. Then, the absorption coefficient α was calculated considering the film thickness d and the film transmittance T_{film} (*eq. (2)*).

$$T_{film} \approx \frac{T_{exp}}{\sqrt{T_{subs}}} \quad (1) \qquad ; \qquad \alpha = \frac{1}{d} ln \frac{1}{T_{film}} \quad (2)\,.$$

Finally, an estimate of the band gap width, E_G, was determined from a plot of

$$(h\nu\alpha) = B(h\upsilon - E_G)^n \quad , \qquad (3)$$

where n = 1/2 is used for $ZnSnN_2$ because it is a semiconductor with direct allowed transitions based on band calculations.[55] B is a constant called the band tailing parameter. The refractive index, n_f, and the extinction coefficient, k_f, were determined using a modified FTIR spectrometer to record reflection-transmission spectra of thin film semiconductor.[56] The constants n_f and k_f were calculated using the optical characterization method of Poruba *et al.*[57] with the following equations

$$k_f = \frac{\alpha\lambda}{4\pi} \quad \text{and} \quad n_f = n_s \frac{1+\sqrt{R_{sfa}}}{1-\sqrt{R_{sfa}}} \quad , \qquad (4)$$

where R_{sfa} is the reflectance of the sample from the substrate side and n_s the substrate refractive index.

FIRST-PRINCIPLE CALCULATIONS

Density functional theory (DFT) geometry relaxation were carried out using the plane-wave Vienna *ab initio* simulation package (VASP).[58,59] The generalized gradient approximation (GGA) in the PBE (Perdew-Burke-Ernzerhof) form was used for the exchange-correlation potential. For the 16-atom orthorhombic unit cell of ZTN, the k-points 9x8x7 Monkhorst-Pack were used for Brillouin-zone integration. All lattice vectors and atomic positions were fully relaxed by minimization of the quantum mechanical stresses and forces using the projector-augmented wave (PAW) method. The cut-off energy for plane-waves was set to 520 eV. For the electronic band structures we used the full-potential linearized augmented plane wave (FLAPW) approach, as implemented in the WIEN2K code.[60] In this method, a plane-wave cutoff corresponding to $R_{MT}K_{max}$= 7 was chosen to avoid overlapping during the band structure calculation. The radial wave functions inside the non-overlapping muffin-tin spheres were expanded up to *lmax* = 12. The charge density was Fourier expanded up to *Gmax* = 16 Å^{-1}. Total energy convergence was achieved with respect to the Brillouin zone (BZ) integration mesh with 500 k-points. Because GGA exchange-correlation functionals are known to underestimate experimental band gaps, we used the modified Becke-Johnson (mBJ) functional which leads to excellent agreement with the experimental values for the energy separation between the highest occupied molecular orbital (HOMO) and the lowest unoccupied molecular orbital (LUMO).[61] We used 5000 k-points in the BZ to compute the band derivatives and the density of states.

RESULTS AND DISCUSSION

Structure and morphology. Table 1 shows the chemical composition of the deposited films synthesized using different bias. Within the deposition conditions described overhead, a quite constant value of the atomic ratio Zn/Zn+Sn is obtained (0.53 ± 0.01) for all the samples.

Table 1. Chemical compositions of $ZnSnN_2$ films prepared at different bias powers.

P_b (W)	Zn (at. %)	Sn (at. %)	N (at. %)	O (at. %)	Zn/(Zn+Sn)
0	25.4	22.0	45.9	6.7	0.54
10	25.7	23.5	48.9	2.0	0.52
20	25.6	23.8	48.5	2.1	0.52
30	25.3	23.3	47.7	3.7	0.52
40	26.3	23.4	46.2	4.1	0.53
50	26.6	24.0	45.7	3.7	0.53

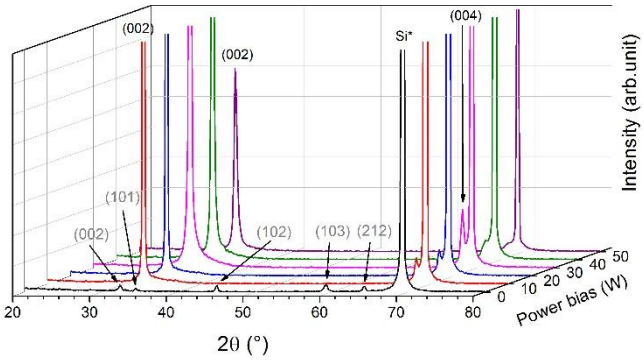

Figure 3. X-ray diffractograms of ZTN films deposited on silicon substrate by varying the bias power from 0 to 50 W.

Table 2. Deposition rate of $ZnSnN_2$ under different substrate bias power (from 0 to 50 W).

	0 W	10 W	20 W	30 W	40 W	50 W
Dep. Rate (± 0.01 nm/s)	0.6	0.56	0.55	0.55	0.52	0.53

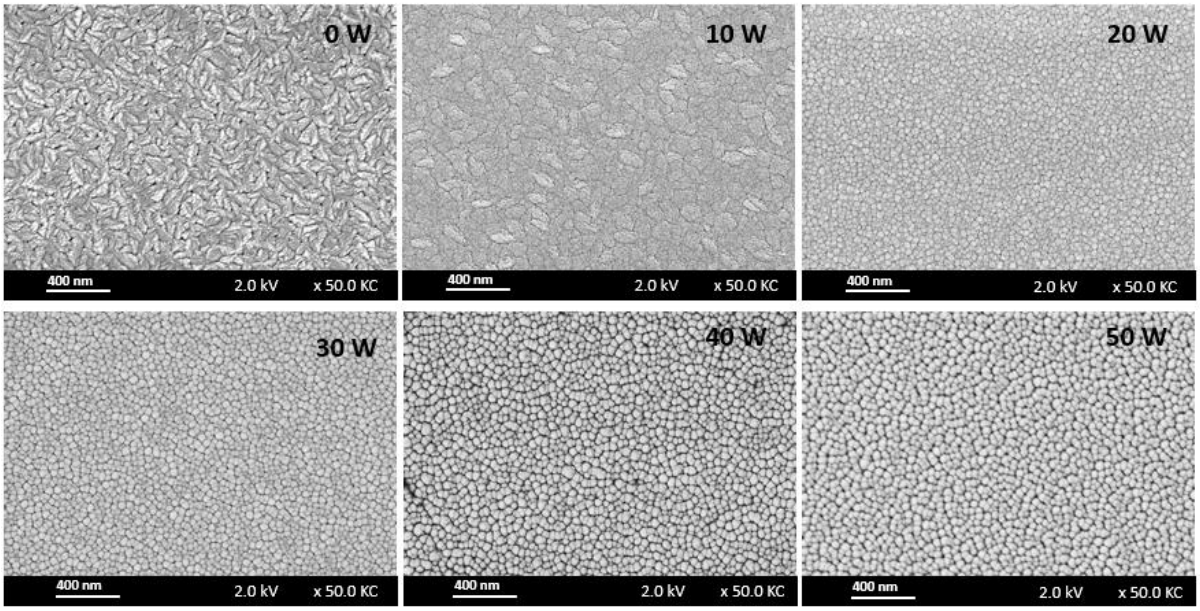

Figure 4. Top surface SEM images of $ZnSnN_2$ films at different bias powers.

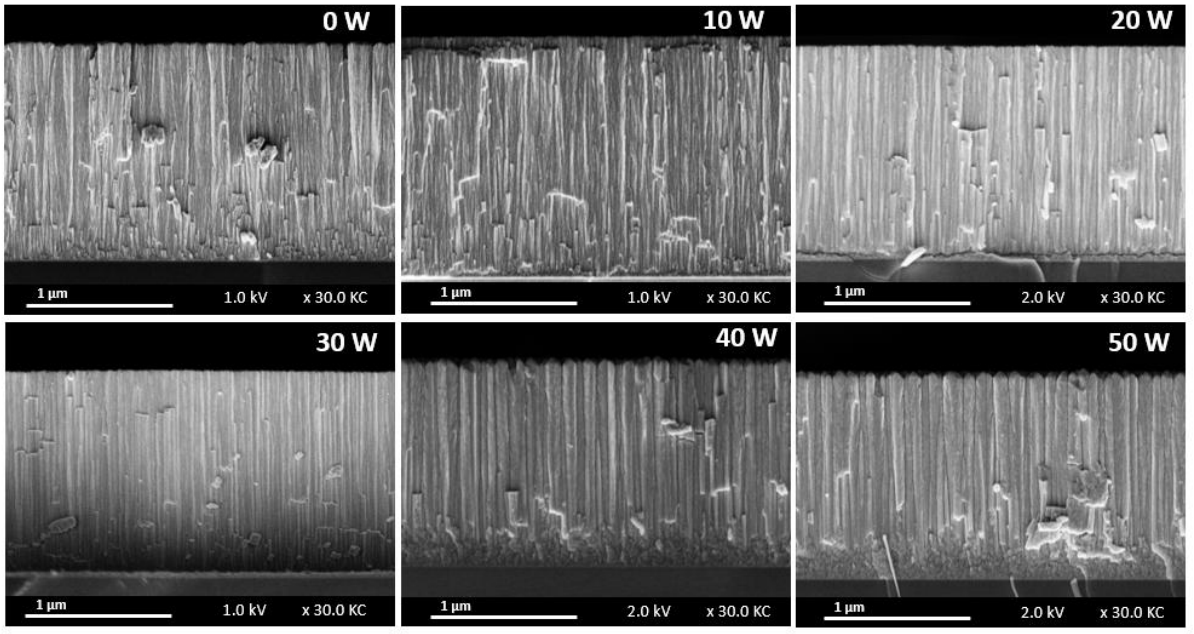

Figure 5. Cross-sectional SEM images of $ZnSnN_2$ films at different bias powers.

Table 3. Experimental lattice parameters based on wurtzite structure deduced from X-ray diffractograms.

	0 W	10 W	20 W	30 W	40 W	50 W
a (Å)	3.405	/	/	/	/	/
c (Å)	5.501	5.504	5.500	5.491	5.503	5.498
Crystallite size (nm)	27	68	60	52	29	20

From these values, it appears that the atomic contents of Zn and Sn slightly increase with the applied bias while the atomic content of oxygen decreases by 3 times, from 6.7 to 2.0 % from 0 W to 20 W bias power. Generally, metal nitride films would contain oxygen from residual oxygen in the growth chamber and adsorbed H_2O and O_2 by the film surface after deposition, under exposure to the ambient air. The decrease of the oxygen concentration of the films under the influence of a bias can be interpreted considering firstly a preferential re-sputtering of oxygen atoms by nitrogen ions during their growth and secondly by their densification limiting their oxidation after growth.

Table 2 confirms the resputtering of the deposited materials due to the energetic ion bombardment.[62,63] In fact, the deposition rate decreases with the increase of the bias power. Even if pure nitrogen is used, then the effect of the bias plays a part in the reduction of the hydrogen content. Different studies on nitrides showed the effect of the bias, in reactive atmosphere, on the decrease of oxygen due to the bias-induced change morphology and the preferential resputtering.[64-67]

Due to the preferential re-sputtering of light elements, the atomic ratio of non-metallic atoms to metallic ones ((N + O) / (Sn + Zn)) decreases from approximately 1.11 (for unbiased film) to 0.98 (50 W). The chemical composition of films deposited on silicon substrates differs slightly from the expected one because of the presence of oxygen: for an unbiased film, the composition $Zn_{1.02}Sn_{0.88}N_{1.84}O_{0.27}$ indicates a possible tin under-stoichiometry but also a nitrogen depletion due to the high oxygen content, compared to a 20 W bias film with $Zn_{1.02}Sn_{0.95}N_{1.94}O_{0.09}$ composition. Consequently, a bias of 10 or 20 W is high enough to reduce the unintentional contamination by oxygen.

The influence of the bias power applied during growth on the film structure was also studied. Figure 3 shows the X-ray diffractograms of highly crystallized thin films on silicon substrate. We have checked that the use of soda lime glass substrate does not affect the film structure. Several results in the literature report that magnetron-sputtering method is a suitable approach to obtain crystallized $ZnSnN_2$ on different substrates at 250 °C, 450 °C and 300 °C, respectively.[19,38,68] The crystal structure of this family of II-IV-N_2 semiconductors is controversial since several structures are proposed : a fully disordered cation sub-lattice correlates with a wurtzite $ZnSnN_2$ structure, whereas some authors claim that the orthorhombic structure with a mixture of two orthorhombic phases $Pna2_1$ and $Pmc2_1$ can lead to disordered materials.[69] In this study, the XRD profile of these samples is consistent with the simulated XRD pattern for the disordered-wurtzite phase (ZnO) $P6_3mc$ structure and with the lattice parameters summarized in Table 3. We observe a transition in the structure of the six samples: the unbiased sample exhibits five peaks of low intensity at 2θ of 32.46°, 34.49°, 45.13°, 59.32° and 64.38°, corresponding to (002), (101), (102), (103) and (212) planes, respectively. By increasing the applied bias power, some peaks disappear and only two peaks are evidenced at 32.46° and 68.09°, corresponding to (002) and (004) planes respectively, which reach their maximum value at 30 W (see Fig. S1 of the Supporting Information). For biased films, the diffractograms exhibit the same strong preferred orientation along the [001] direction indicating that the bias has a favorable effect on the preferential orientation of the ZTN films. Furthermore, it remains challenging to determine the film structure based on these data. Only two peaks near 20°, corresponding to (110) and (011) planes could be used to differentiate the orthorhombic $Pna2_1$ structure from the hexagonal one. However, these peaks are not observed in this region. It can be due to either a very weak intensity of these peaks or to the cation disorder of the sublattice.[30]

It underlines that further investigations are necessary to confirm the structure of this series of ZTN films. The *a* and *c* lattice parameters have been extracted (Table 3) from the X-ray diffractograms reported in Fig. 3. Due to the strong preferential orientation of our films the *a* lattice parameter value could be obtained only for the unbiased sample. The *c* lattice parameter value, which was obtained rather accurately, can be compared with the values reported by Lahourcade *et al*, Deng *et al*. and Kawamura *et al*. that is 5.52 ± 0.01 Å, 5,498 Å and 5.464 Å, respectively.[19-21] The theoretical work of Senabulya *et al*. predicts *c* = 5.542 Å, referenced to the $Pna2_1$ symmetry group with the PBE function.[69] The *c* parameter is the most accurate due to the strong preferential orientation in our films. The crystallite size was calculated by Scherrer's equation with a *K* factor of 0.9. We observe that the crystallite size increases up to about 68 nm when a 10 W bias is applied and then decreases with the bias power up to approximately 20 nm for the 50 W bias sample.

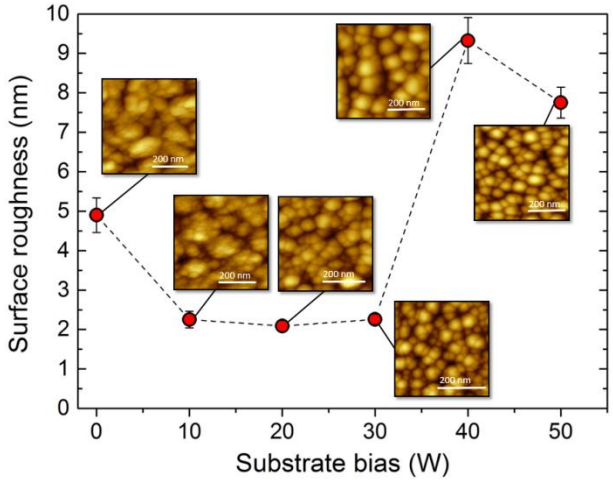

Figure 6. Surface roughness (1 µm² analysis) of $ZnSnN_2$ films deposited using different bias powers with corresponding AFM images.

Figs. 4 and 5 display the SEM images of the ZTN films deposited on silicon substrates with different bias powers. By combining top and cross-sectional views, it is highlighted that the application of a bias on the substrate changed the morphology of the films. As in previous works,[27,36,68] the same microstructure of $ZnSnN_2$ is observed: all the films exhibit a columnar structure. However, two phenomena seem to compete. On the one hand, the column width seems to increase with the power bias, inducing a decrease of the number of grain boundaries and, from 0 W to 30 W applied power, the films become denser and smoother. On the other hand, the shape of the column surface changes as the bias power is increased, moving from non-faceted to faceted grains. This result is clearly distinguishable on the surface images of the 40 W and 50 W biased samples. It is also relevant to notice that these higher bias powers alter the densification of the films.

This is why we believe that the reduction of oxygen concentration with increasing bias power at low powers is counterbalanced at high powers by its higher diffusion through those wider grain boundaries (Table 1) favoring its incorporation. Adding to these observations, atomic force microscopy (AFM) analyses have been performed to get more quantitative information on the film roughness. The surface morphologies evidenced by AFM are quite similar to those observed by SEM. The roughness of the films has been summarized in Figure 6. The AFM results confirm the observation made in the SEM images, *i.e.* a minimum value of 2.1 nm RMS surface roughness is noticed at 20 W bias power and an increase by a factor 4 to 5 is observed for the higher bias power range. We also observed the same trends for a larger scale of AFM images, which confirmed the homogeneous morphology og these films (see SI figure S2). These values are similar to those reported in a previous work using combinatorial RF magnetron sputtering with R_q around ~4.5 nm.[35] This rough surface may arise from the resputtering effect, which is due to the bombardment of high-energy ions from the plasma.[5] The same trend has been reported by Han Kim *et al.* for silicon nitride, where both a surface roughness 4 times lower and a transition from an open columnar structure to a dense smooth film were observed when applying a bias.[64]

The microstructure of unbiased, 20, 40 and 50 W biased films has been characterized by TEM in cross section (Fig. 7). Columnar microstructure observed by SEM (Fig. 5) is clearly confirmed by TEM micrographs for all the samples (Figs. 7a, b, d, f, S3 and S4). This columnar microstructure is a well-known structure of sputtered $ZnSnN_2$ films and more generally of sputtered nitride compounds.[70]

The width of the columns for the unbiased sample is ranging between 10 and 95 nm with a large heterogeneity of grain size along the film thickness (small close to the film-substrate interface and large close to the film top surface, Fig. 7a). With increasing bias power the column width becomes more homogeneous (~ 60 nm at 20 W, Fig. 7b), homogeneity that decreases at higher biases (see Fig. 7d for 40 W of bias). Two representative electron diffraction patterns are added and indexed considering a [100] zone axis (Figs. 7c, 7e). These diffraction patterns validate the growth direction along the *c*-axis evidenced by X-ray diffraction. Since diffraction spots are seen in the SAED pattern, each column can be considered as a single crystal for the 20 W bias film. The 50 W bias film exhibits a microstructure different from that observed for lower bias values (Fig. 7f). Indeed, a dense interlayer of 70 nm of polycrystalline ZTN appears close to the substrate and a 250 nm thick layer, which also contains small grains, is observed above it. Finally, a columnar ZTN is evidenced. Such a disordered microstructure may be explained considering that the impinging nitrogen ions have a too high energy disturbing the nucleation of ZTN columns.

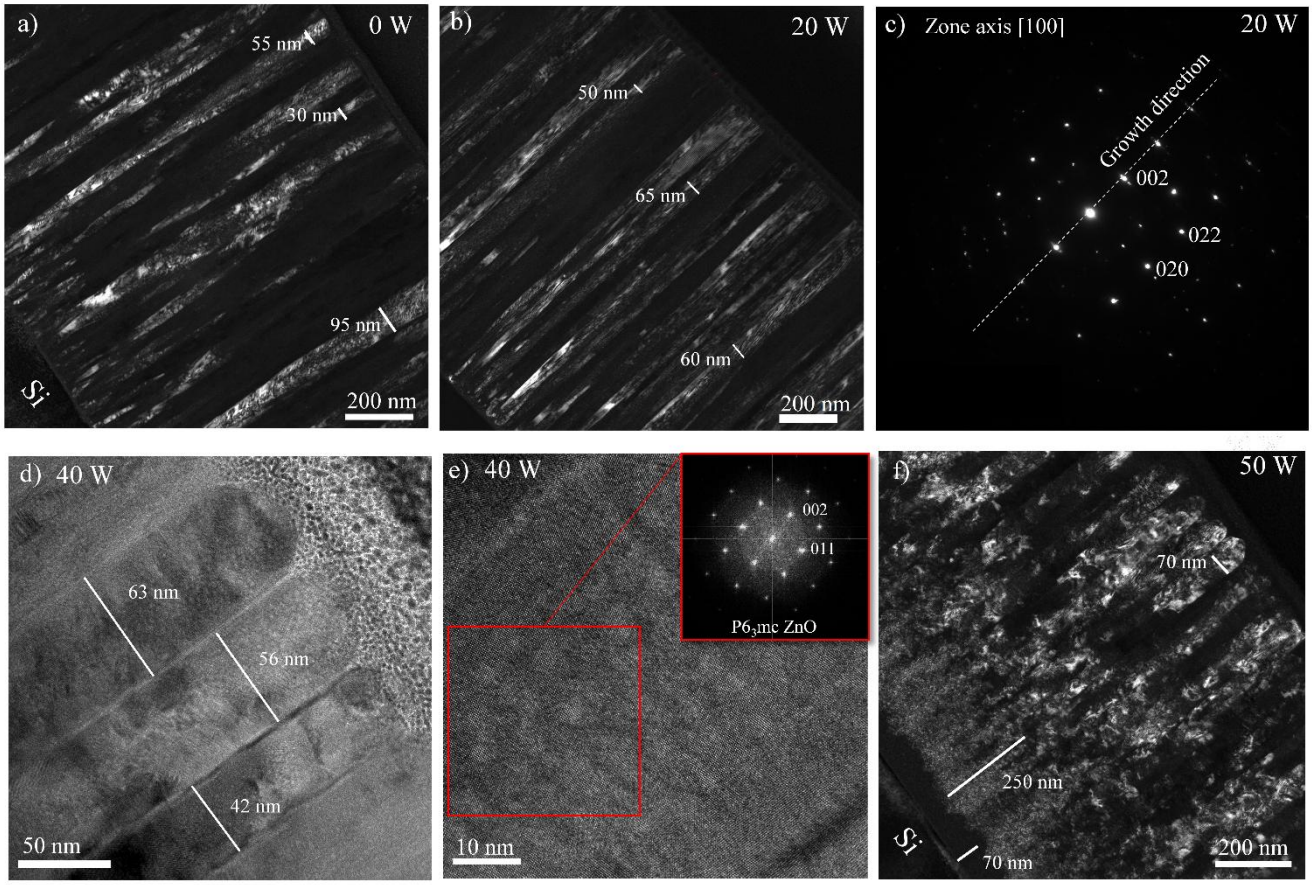

Figure 7. TEM characterization of ~1.3 µm thick films deposited on silicon substrate using the following bias powers unbiased, 20, 40 and 50 W. (a), (b) and (f) Dark field image obtained with the 002 spot. (c) Electron micro-diffraction pattern on one column in the 20 W film along [100] zone axis. (d) HRTEM of the columnar surface on the 40 W sample. (e) HRTEM of a column on the 40 W sample. The inset shows the FFT (Fast Fourier Transform) from the red box.

EDS analyses in STEM mode have been completed on the 20 W bias film to study the atomic element concentrations along a horizontal line profile across some columns (Figs. 8a and b). In a previous work on unbiased ZTN by Alnjiman *et al.* a nitrogen depletion was observed at the column boundaries while the oxygen concentration increases up to 12 at.%.[29]

This excess of oxygen concentration can be explained by an oxidation coming from the diffusion of oxygen molecules into the grown film under ambient air exposure. In the present study, by applying a 20 W bias, we succeeded in reducing the oxygen content at the grain boundaries by densifying the film. In fact, the composition of the layer remains the same along the EDS transversal acquisition line.

Optical properties of $ZnSnN_2$. The transmittances in the UV-visible NIR range of the different samples are depicted in Fig. 9. Transmittance shows a strong variation in the absorption threshold as the bias power increases with a red-shift of the absorption edge and, for 30 W bias and above, the films are transparent in the visible region. The multiple interference fringes are due to multiple reflections by the different interfaces: air, $ZnSnN_2$ layer and glass substrate. We observe two different behaviors : first of all, the unbiased and 10 W biased samples show a transmittance decreasing for wavelengths higher than 1500 nm. This absorption could be due to the presence of free carriers responsible for plasmon resonance effects. However, the films up to 20 W bias exhibit a constant transmittance after 1500 nm, which corresponds to a semicon-

ductor behavior. By increasing the bias power, up to 50 W, a new type of behavior appeared with a slow increase in transmittance between 1000 and 2500 nm (limit of wavelength measurement). For direct band gap material, a very abrupt increase in transmittance is expected when the photon energy reaches the gap energy value.

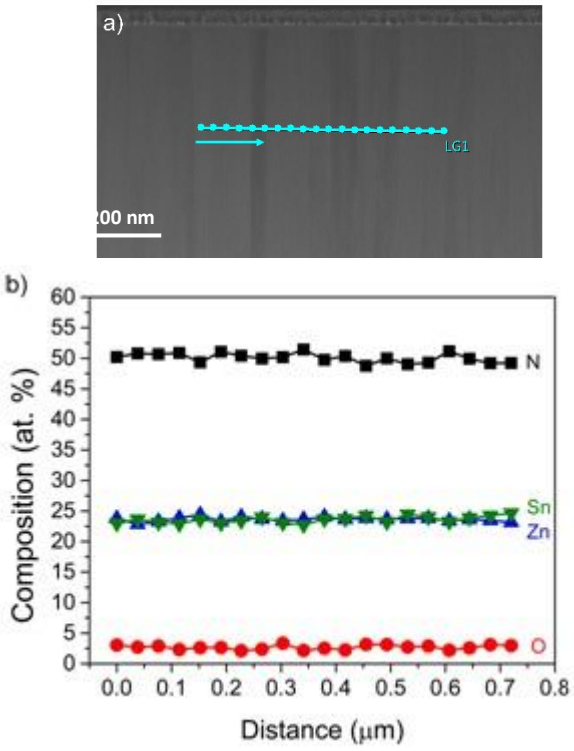

Figure 8. a) Annular dark field - STEM image of the 20 W $ZnSnN_2$ thin film. The blue dots on the line indicate the positions of EDS measurements. b) Corresponding transversal chemical composition along the line.

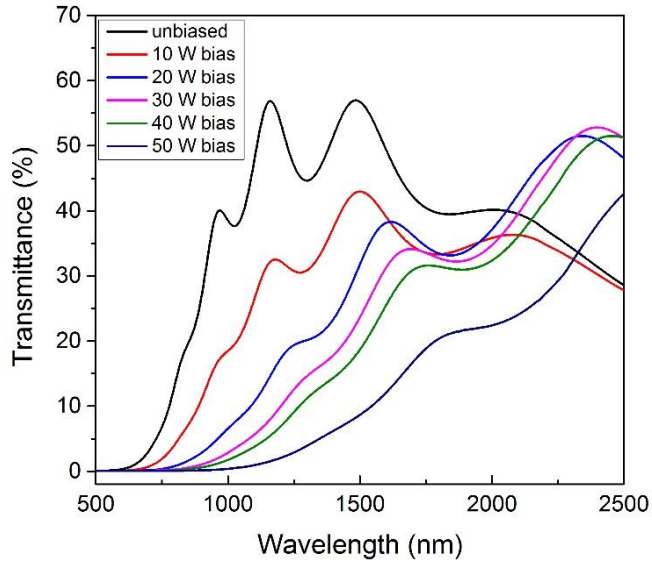

Figure 9. Transmittance spectra of the $ZnSnN_2$ films deposited on glass substrate for the different applied bias powers.

For the samples deposited at biases of 20 W and higher, a slow increase of the transmittance with wavelength is observed. We can attribute this behavior to the presence of band tails created by disordered phases (microcrystalline or amorphous) of the materials. Such disordered phases are observed in the SEM picture of Fig. 5 for samples deposited with bias power higher than 30 W. The impact of the band tails is also observed on the exponential increase of the absorption coefficient with increasing energy of the incident light (see SI Fig. S5). Besides, a decrease of the transmittance at large wavelengths is observed for the 0 at 10 W samples that can be attributed to intra band transitions.

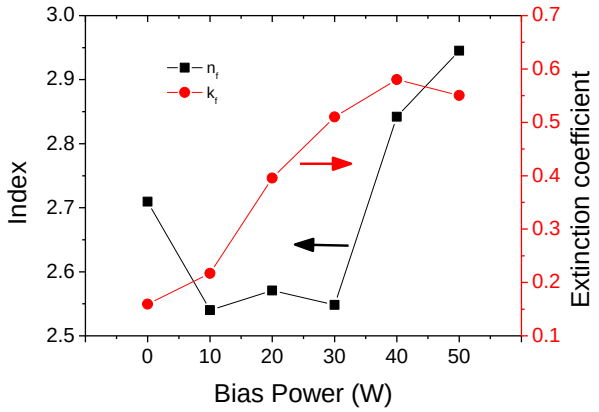

Figure 10. Optical parameters n_f and k_f at 730 nm for film biases between 0 and 50 W deduced from UV-Vis. transmittance data.

Figure 10 represents the refractive index and extinction coefficient values determined at the wavelength λ = 730 nm (1.7 eV, *i.e.* just above the highest band gap) using an FTIR spectrophotometer. The refractive index decreases from 2.7 down to 2.54 with increasing bias power up to 30 W. Then, we observe an increase, up to 2.95, for higher bias powers. This evolution of the refractive index may be linked to evolution of the compactness of the material with the deposition conditions.[71] The reduction of the refractive index could then be explained by the increase of the grain size and a better homogeneity of the material at low bias power. Javaid *et al.* reported the same phenomenon with a decrease of the refractive index from ~ 2.43 to 2.30 at 730 nm for as-deposited an annealed ZTN.[2] Another study on the effect of the deposition temperature reported a refractive index of ~ 2.45 at the wavelength of 730 nm for an as-deposited film.[20] However, the extinction coefficient, that is the imaginary part of the refractive index: $\underline{n}_f = n_f + ik_f$, is linked to the absorption coefficient. At 730 nm the absorption coefficient raises and so does the extinction coefficient, from 0.16 to 0.58. If we compare those values of optical constants with the calculated ones using WIEN2k (see SI Fig. S6), we can notice a rather good agreement of calculated values with those of the film deposited at 10 W. At 730 nm, the calculated refractive index and extinction coefficient are 2.43 and 0.23, respectively. (see SI Fig. S7).

The effect of the bias power on the band gap is depicted in Figure 11a. The determination of the band gap energy is given by the intercept of the linear extrapolation of the curve $(\alpha h\nu)^2$ versus photon energy to the abscissa axis (see SI Fig. S8).[72] As a function of the bias power, the band gap evolves in the 1.34 – 1.7 eV range. When the bias power increases, the band gap energy clearly decreases progressively to reach a value close to E_G = 1.37 eV calculated by DFT with a hybrid functional (mbj) represented on the band structure and the corresponding PDOS (Figs. 11b,c). These calculations were performed with the Wien2K code using a functional based on the optimized effective potential method (OEP). The calculations are solved

with a number of points k = 3000 within the Brillouin zone. The band structure calculations confirm the direct band gap of $ZnSnN_2$ with valence band maximum (VBM) and conduction band minimum (CBM) located at the Γ point of the Brillouin zone. The projected density of states (PDOS) is represented in Fig. 11b. We can deduce that the top of the valence band maximum mainly results from the hybridization of N 2p and Zn 3d states, while the minimum of the conduction band is dominated by N 2s and 2p and Sn 5s orbitals. The particularity, found by Pandey *et al.*, that a highly dispersive isolated band constructs the CBM, is observed on the band structure.[8]

The difference between theoretical and experimental values of the optical band gap could be attributed to the Burstein-Moss effect as it was in InN[48] (Fig. 11d). Indeed, the excess of electron carrier concentration in some degenerate semiconductor pushes the Fermi energy level in the conduction band The excess of electrons populating this band leads to intra band transitions for low photon energy resulting in a decrease of the transmittance at large wavelengths as observed for the 0 and 10 W biases. The use of bias during the growth reduces the oxygen contamination and then may contribute to reduce this Burstein-Moss shift of the apparent band gap down to the theoretical band gap energy prediction. This assumption concerning the Burstein-Moss effect, associated with different doping levels and/or strains in the samples, has been proposed by Lahourcade *et al.* for the same nitrides materials.[19] However, the Burstein-Moss effect cannot explain the decrease of the band gap observed for the sample deposited with a bias of 50 W.

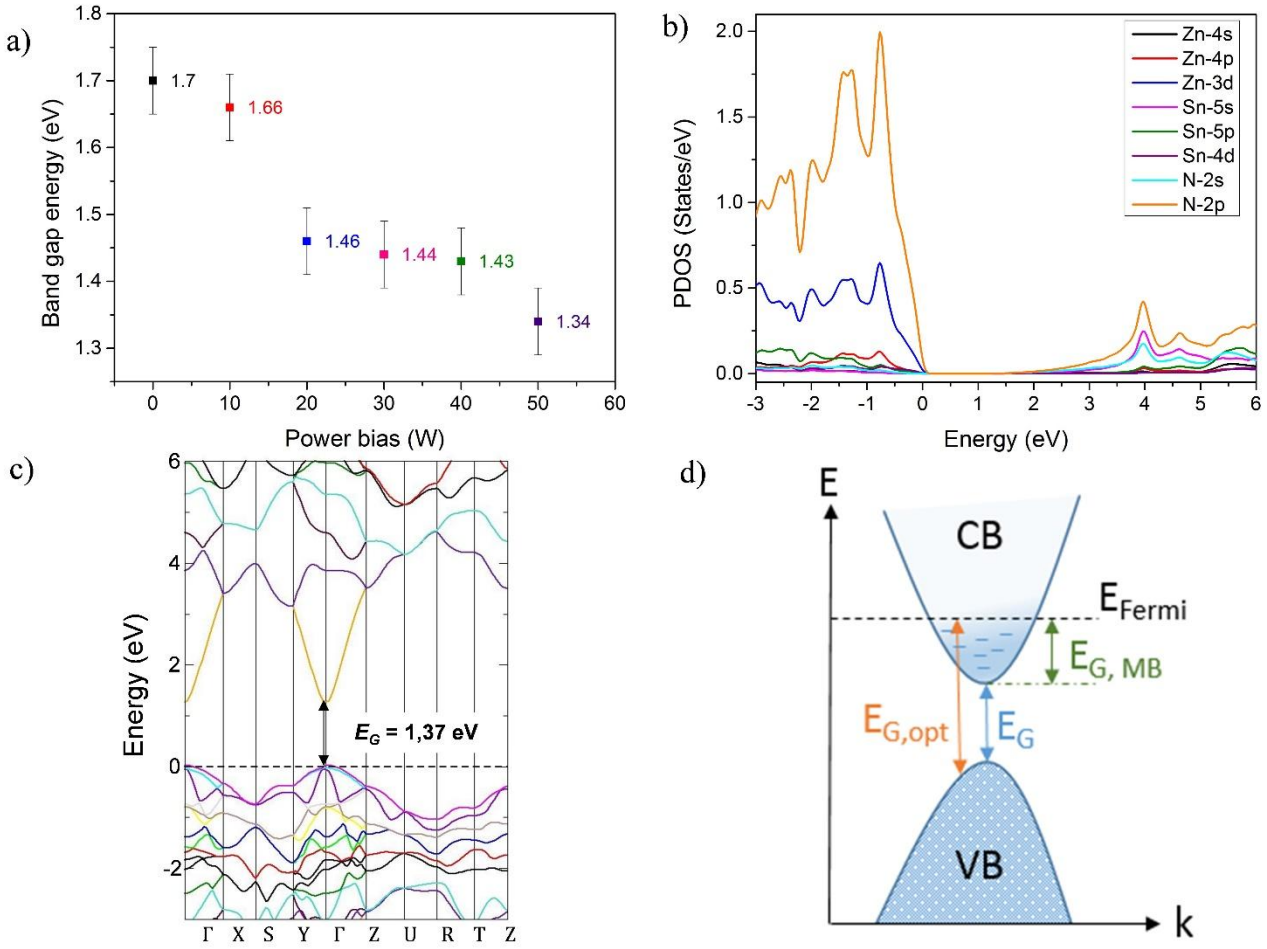

Figure 11. a) Band gap energy determined by Tauc plots. b) Projected density of States (PDOS) of $ZnSnN_2$. c) Electronic band structure of $ZnSnN_2$. d) Schematic illustration of the Burstein–Moss shift in the apparent band gap caused by an excess of electrons.

Table 3. Hall Effect measurement results of the samples on silicon substrate depending on applied bias power. The activation energy values are deduced from I-V experiments vs temperature in planar configuration.

P_b (W)	TYPE	n (cm^{-3})	σ (Scm^{-1})	μ ($cm^2V^{-1}s^{-1}$)	E_a (meV)
0	n-type	$(3.30\pm2.23)\times10^{18}$	1.47±0.01	2.8±1.1	38±1
10	n-type	$(1.13\pm0.22)\times10^{18}$	2.22±0.01	12.6±2.5	63±1
20	n-type	$(1.07\pm0.02)\times10^{17}$	0.68±0.01	39.6±0.6	88±1
30	n-type	$(2.25\pm0.06)\times10^{17}$	0.25±0.02	6.9±0.2	94±1
40	n-type	$(1.34\pm0.37)\times10^{18}$	0.26±0.02	1.2±0.3	105±1
50	n-type	$(5.05\pm0.32)\times10^{17}$	0.57±0.01	7.0±0.5	98±1

Electrical properties of $ZnSnN_2$. The electrical properties have been measured by Hall effect at room temperature and by I-V experiments in planar configuration for several temperatures. These measurements provide information on the type of material (n or p), on the density and mobility of the associated free carriers as well as on the activation energy. The results of the Hall measurements are summarized in Table 4. The well-known n-type of the ZTN was confirmed for all the films. The charge carrier concentration of biased $ZnSnN_2$ thin films exhibits a minimum value of 1.1×10^{17} cm^{-3} for a bias power of 20 W which is almost one decade lower than obtained under the unbiased condition. This result confirms the assumption stated in the previous paragraph: the electron concentration n in the conduction band has been reduced by adding a bias during deposition. The electron mobility, μ, also shows a maximum at 20 W with a high value of ~ 40 $cm^2V^{-1}s^{-1}$. The conductivity, σ, decreases from 1.43 to 0.25 Scm^{-1} from 0 W to 30 W bias films and increases up to 0.57 Scm^{-1} at 50 W.

The electrical properties of $ZnSnN_2$ were controversed in the previous literature and vary in a wide scope. In 2013, Lahourcade *et al.* gave a first approximation of electron concentration on RF films sputtered ranging from ~ 5×10^{19} cm^{-3} to ~ 1×10^{21} cm^{-3}.[19] The same year, Feldberg *et al.* obtained PAMBE-grown $ZnSnN_2$ films with free electron density in a narrower range from ~3×10^{20} cm^{-3} to ~1×10^{21} cm^{-3}, and reported a mobility of 10 $cm^2.V^{-1}.s^{-1}$.[24] Finally, in 2016, Qin *et al.* succeed to decrease the carrier concentration of DC magnetron sputtering films to ~7×10^{17} cm^{-3} after a 350 °C post annealing treatment.[27] In the different references, there is no detailed information regarding the duration between the films synthesis and the electrical properties measurements or the samples storage conditions before the electrical measurements. In the present study, we observed that the conductivity values change during the first days after synthesis. This non-reported phenomenon should require further information.

The conductivity σ of all the samples was also measured at room temperature using I-V experiments in planar configuration. The evolution of the conductivity according to the bias power is in good agreement with Hall effect measurements (see SI Fig. S9). Then, the temperature dependence of σ was measured under vacuum in the range 200-450 K with a 10 K step. At all the temperatures we have observed an Ohmic behavior of the contacts. Two different conduction mechanisms were found. Below 300 K the predominant mechanism of conduction is clearly 3D variable range hopping between localized states in the vicinity of the Fermi level whereas above 300 K the conductivity is dominated by transport of carriers in the extended states. The variable range hopping is characterized by a variation of the conductivity following the equation[73]

$$\sigma(T) = \sigma_{00}\exp\left[-\left(T/T_0\right)^{1/4}\right] \quad . \qquad (5)$$

SI Fig. S9 shows that, indeed, we observe this regime of transport at low temperature in the films under study. Above 300 K the dominant transport path seemed to be via free carriers in the extended states and the conductivity follows an Arrhenius law[74]

$$\sigma(T) = \sigma_0 exp\left[-(E_c - E_F)/k_bT\right] \quad . \qquad (6)$$

The films being n-type, from this measurement the activation energy $E_a = E_c - E_F$, can be extracted. SI Fig. S11 displays the variations of the conductivities of the films with temperature following an Arrhenius plot. For the unbiased sample, the conductivity exhibits a weak evolution with temperature with a very low E_a value of 40 meV whereas for the samples biased at powers higher than 20 W, a significant temperature dependence is observed with an E_a value around 0.10 eV (see Table 4 and SI Fig. S12). In this range of bias powers E_a remains constant suggesting a Fermi Level pinning due to the density of state in the band tails. These results confirm the optical measurements conclusions that for 0 and 10 W, the Fermi level is very close to the conduction band, leading to a high population of electrons inducing extra absorption at long wavelengths, whereas for bias powers of 20 W and above, the Fermi level moves deeper in the gap, away from the conduction band, suppressing this effect.

These very low activation energies measured at low applied biases suggest that the deposited films are degenerated. The conduction band is therefore highly populated and it explains the decrease of the transmittance for high wavelengths due to intra band transitions. It suggests also that the Fermi level is not located in the conduction band. This fact is reinforced by the observation of 3D variable range hopping at low temperatures for all the films. Indeed, if the Fermi level was pinned in the extended states we would not observe such a hopping transport. Therefore, it seems difficult to invoke the Burstein-Moss effect to explain the large band gaps observed at 0 W and 10 W of bias. The evolution with the bias power of the structure of the material, orthorhombic, hexagonal or a mixture of both, combined with an evolution of the disorder, could be an alternative explanation of the gap evolution from 0 W to 20 W applied bias as well as from 40 W to 50 W applied bias where the gap drops from 1.42 eV down to 1.34 eV.

CONCLUSION

The influence of the bias power on the microstructure, composition, and optoelectronic properties of the deposited ZnSnN2 thin films has been highlighted.

In a small range of bias powers (10 to 30 W), we obtain films with a better homogeneity of the columnar structure, larger crystallites, a higher compactness, a smoother surface, and a low and homogeneously distributed oxygen content. We also have observed a decrease of the band gap that reaches the expected value from ab initio calculations. With a small bias power (20 W), the lowest value of the electron density associated with the highest mobility value have been obtained.

However, the applied bias power does not minimize the disorder of the material responsible for the presence of large band tails. In addition, large bias values are even responsible for the presence of disordered phases at the beginning of the deposition. This disorder certainly has an impact on the transport properties and more work is needed in the future to gain better control of it.

Despite this issue, the use of bias power definitely has a positive impact on material quality. The encouraging results regarding the optical and electrical properties confirm that the application of bias power at room temperature may allow this semiconductor to reach the expectations predicted by the preliminary theoretical studies. Moreover, it seems like a 20 W power bias is the optimal parameter to obtain a compromise between the best microstructural and optoelectronic properties.

ASSOCIATED CONTENT

The Supporting Information is available free of charge at https://pubs.acs.org/doi/10.1021/acsaelm.1c00478.

Figure S1, X-ray diffractograms of ZTN films deposited with different bias powers; Figure S2, AFM images of ZnSnN2 films; Figure S3, TEM micrographs of ~1.3 µm thick unbiased and 20 W bias films; Figure S4, TEM micrographs of ~1.3 µm thick 40 W and 50 W bias films; Figure S5, optical absorption coefficients for biased films; Figure S6, calculated absorption coefficient of ZSN; Figure S7, calculated refractive index and extinction coefficient of ZTN; Figure S8, Tauc plot of ZnSnN2 bias films; Figure S9, evolution of the sample conductivity; Figure S10, conductivity of the material deposited under different biases; Figure S11, Arrhenius plots of the conductivities of the materials; and Figure S12, evolution of the activation energy with bias power

(PDF)AUTHOR INFORMATION

Corresponding Author

* E-mail : jean-françois.pierson@univ-lorraine.fr, Tel : +33 372 74 25 99.

Author Contributions

‡ A.V. and F.A. contributed equally to this work.

ACKNOWLEDGMENTS

This work has been funded by the ANR-17-CE05-0022 OPERA project and the Contrat de Plan Etat-Région MatDS. High Performance Computing resources were provided by the EXPLOR centre hosted by the Université de Lorraine. The Centre de Compétences Daυm, X-γ and Optique Laser of the Institut Jean Lamour are acknowledged for the access to their equipments. The authors would like to thank E. Gaudry of the Institut Jean Lamour and R. Al Rahal Al Orabi of Solvay, Design and Development of Functional Materials Department, for their computational skills and useful advices.

REFERENCES

(1) Paudel, T. R.; Lambrecht, W. R. L. First-Principles Study of Phonons and Related Ground-State Properties and Spectra in Zn-IV-N $_2$ Compounds. *Phys. Rev. B* **2008**, *78* (11), 115204.

(2) Javaid, K.; Yu, J.; Wu, W.; Wang, J.; Zhang, H.; Gao, J.; Zhuge, F.; Liang, L.; Cao, H. Thin Film Solar Cell Based on $ZnSnN_2$ /SnO Heterojunction. *Phys. Status Solidi RRL - Rapid Res. Lett.* **2018**, *12* (1), 1700332.

(3) Arca, E.; Fioretti, A.; Lany, S.; Tamboli, A. C.; Teeter, G.; Melamed, C.; Pan, J.; Wood, K.; Toberer, E.; Zakutayev, A. Band Edge Positions and Their Impact on the simulated device performance of $ZnSnN_2$ based solar cells, *IEEE J. Photovolt.* **2018**, 8 (1), 110-117.

(4) Javaid, K.; Wu, W.; Wang, J.; Fang, J.; Zhang, H.; Gao, J.; Zhuge, F.; Liang, L.; Cao, H. Band Offset Engineering in $ZnSnN_2$-Based Heterojunction for Low-Cost Solar Cells. *ACS Photonics* **2018**, *5* (6), 2094–2099..

(5) Cao, X.; Kawamura, F.; Ninomiya, Y.; Taniguchi, T.; Yamada, N. Conduction-Band Effective Mass and Bandgap of $ZnSnN_2$ Earth-Abundant Solar Absorber. *Sci. Rep.* **2017**, *7* (1), 14987.

(6) Punya, A.; Paudel, T. R.; Lambrecht, W. R. L. Electronic and Lattice Dynamical Properties of II-IV-N2 Semiconductors. *Phys. Status Solidi C* **2011**, *8* (7–8), 2492–2499.

(7) Narang, P.; Chen, S.; Coronel, N. C.; Gul, S.; Yano, J.; Wang, L.-W.; Lewis, N. S.; Atwater, H. A. Bandgap Tunability in Zn(Sn,Ge)N_2 Semiconductor Alloys. *Adv. Mater.* **2014**, *26* (8), 1235–1241.

(8) Pandey, M.; Kuhar, K.; Jacobsen, K. W. II–IV–V_2 and III–III–V_2 Polytypes as Light Absorbers for Single Junction and Tandem Photovoltaic Devices. *J. Phys. Chem. C* **2017**, *121* (33), 17780–17786.

(9) Veal, T. D.; Feldberg, N.; Quackenbush, N. F.; Linhart, W. M.; Scanlon, D. O.; Piper, L. F. J.; Durbin, S. M. Band Gap Dependence on Cation Disorder in $ZnSnN_2$ Solar Absorber. *Adv. Energy Mater.* **2015**, *5* (24), 1501462.

(10) Martinez, A. D.; Fioretti, A. N.; Toberer, E. S.; Tamboli, A. C. Synthesis, Structure, and Optoelectronic Properties of II–IV–V_2 Materials. *J. Mater. Chem. A* **2017**, *5* (23), 11418–11435.

(11) Feldberg, N.; Keen, B.; Aldous, J. D.; Scanlon, D. O.; Stampe, P. A.; Kennedy, R. J.; Reeves, R. J.; Veal, T. D.; Durbin, S. M. $ZnSnN_2$: A New Earth-Abundant Element Semiconductor for Solar Cells. In *2012 38th IEEE Photovoltaic Specialists Conference*; IEEE: Austin, TX, USA, 2012; pp 002524–002527.

(12) Punya, A.; Lambrecht, W. R. L.; van Schilfgaarde, M Quasiparticle Band Structure of Zn-IV-N_2 Compounds. *Phys. Rev.B: Condens. Matter Mater. Phys.* **2011**, 84 (16), 165204.

(13) Punya, A.; Lambrecht, W. R. L. Band Offsets between ZnGeN 2, GaN, ZnO, and $ZnSnN_2$ and Their Potential Impact for Solar Cells. *Phys. Rev. B: Condens. Matter Mater. Phys.* **2013**, 88 (7), 075302.

(14) Chen, S.; Narang, P.; Atwater, H. A.; Wang, L.-W. Phase Stability and Defect Physics of a Ternary ZnSnN2 Semiconductor: First Principles Insights. *Adv. Mater.* **2014**, 26 (2), 311−315.

(15) Fang, D. Q.; Zhang, Y.; Zhang, S. L. Band Gap Engineering of $ZnSnN_2$ /ZnO (001) Short-Period Superlattices via Built-in Electric Field. *J. Appl. Phys.* **2016**, 120 (21), 215703.

(16) Lany, S.; Fioretti, A. N.; Zawadzki, P. P.; Schelhas, L. T.; Toberer, E. S.; Zakutayev, A.; Tamboli, A. C. Monte Carlo Simulations of Disorder in ZnSnN2 and the Effects on the Electronic Structure. *Phys. Rev. Mater.* **2017**, 1 (3), 035401.

(17) Khan, I.; Heinselman, K.; Zakutayev, A. Review of $ZnSnN_2$ Semiconductor Material. *J. Phys. Energy* **2020**, 2 (3), 032007.

(18) Quayle, P. C.; He, K.; Shan, J.; Kash, K. Synthesis, Lattice Structure, and Band Gap of $ZnSnN_2$. *MRS Commun.* **2013**, *3* (3), 135–138.

(19) Lahourcade, L.; Coronel, N. C.; Delaney, K. T.; Shukla, S. K.; Spaldin, N. A.; Atwater, H. A. Structural and Optoelectronic Characterization of RF Sputtered $ZnSnN_2$. *Adv. Mater.* **2013**, *25* (18), 2562–2566.

(20) Deng, F.; Cao, H.; Liang, L.; Li, J.; Gao, J.; Zhang, H.; Qin, R.; Liu, C. Determination of the Basic Optical Parameters of $ZnSnN_2$. *Opt. Lett.* **2015**, *40* (7), 1282.

(21) Kawamura, F.; Yamada, N.; Imai, M.; Taniguchi, T. Synthesis of $ZnSnN_2$ Crystals via a High-Pressure Metathesis Reaction: Synthesis of $ZnSnN_2$ Crystals via a High-Pressure Metathesis Reaction. *Cryst. Res. Technol.* **2016**, *51* (3), 220–224.

(22) Kuo, C.-H.; Chang, K.-S. Piezotronic and Piezophototronic Properties of Orthorhombic $ZnSnN_2$ Fabricated Using Zn–Sn_3N_4 Composition Spreads through Combinatorial Reactive Sputtering. *Cryst. Growth Des.* **2017**, *17* (9), 4694–4702.

(23) Le, D. D.; Ngo, T. S.; Song, J.-H.; Hong, S.-K. Epitaxial Growth of Bandgap Tunable $ZnSnN_2$ Films on (0001) Al $_2$ O $_3$ Substrates by Using a ZnO Buffer. *Cryst. Growth Des.* **2018**, *18* (3), 1385–1393.

(24) Feldberg, N.; Aldous, J. D.; Linhart, W. M.; Phillips, L. J.; Durose, K.; Stampe, P. A.; Kennedy, R. J.; Scanlon, D. O.; Vardar, G.; Field, R. L.; Jen, T. Y.; Goldman, R. S.; Veal, T. D.; Durbin, S. M. Growth, Disorder, and Physical Properties of $ZnSnN_2$. *Appl. Phys. Lett.* **2013**, *103* (4), 042109.

(25) Quayle, P. C.; Blanton, E. W.; Punya, A.; Junno, G. T.; He, K.; Han, L.; Zhao, H.; Shan, J.; Lambrecht, W. R. L.; Kash, K. Charge-Neutral Disorder and Polytypes in Heterovalent Wurtzite-Based Ternary Semiconductors: The Importance of the Octet Rule. *Phys. Rev. B* **2015**, *91* (20), 205207.

(26) Fioretti, A. N.; Zakutayev, A.; Moutinho, H.; Melamed, C.; Perkins, J. D.; Norman, A. G.; Al-Jassim, M.; Toberer, E. S.; Tamboli, A. C. Combinatorial Insights into Doping Control and Transport Properties of Zinc Tin Nitride. *J. Mater. Chem. C* **2015**, *3* (42), 11017–11028.

(27) Qin, R.; Cao, H.; Liang, L.; Xie, Y.; Zhuge, F.; Zhang, H.; Gao, J.; Javaid, K.; Liu, C.; Sun, W. Semiconducting $ZnSnN_2$ Thin Films for Si/$ZnSnN_2$ p-n Junctions. *Appl. Phys. Lett.* **2016**, *108* (14), 142104

(28) Shing, A. M.; Tolstova, Y.; Lewis, N. S.; Atwater, H. A. Effects of Surface Condition on the Work Function and Valence-Band Position of $ZnSnN_2$. *Appl. Phys. A* **2017**, *123* (12), 735.

(29) Alnjiman, F.; Diliberto, S.; Ghanbaja, J.; Haye, E.; Kassavetis, S.; Patsalas, P.; Gendarme, C.; Bruyère, S.; Cleymand, F.; Miska, P.; Boulet, P.; Pierson, J. F. Chemical Environment and Functional Properties of Highly Crystalline $ZnSnN_2$ Thin Films Deposited by Reactive Sputtering at Room Temperature. *Sol. Energy Mater. Sol. Cells* **2018**, *182*, 30–36.

(30) Cai, X.-M.; Wang, B.; Ye, F.; Zeng, J.-J.; Vaithinathan, K.; Wang, F.; Ma, X.-F.; Xie, Y.-Z.; Zhang, D.-P.; Fan, P.; Roy, V. A. L. Fabricating $ZnSnN_2$ with Cosputtering. *Surf. Coat. Technol.* **2019**, *359*, 169–174.

(31) Fioretti, A. N.; Pan, J.; Ortiz, B. R.; Melamed, C. L.; Dippo, P. C.; Schelhas, L. T.; Perkins, J. D.; Kuciauskas, D.; Lany, S.; Zakutayev, A.; Toberer, E. S.; Tamboli, A. C. Exciton Photoluminescence and Benign Defect Complex Formation in Zinc Tin Nitride. *Mater. Horiz.* **2018**, *5* (5), 823–830.

(32) Hsu, A.-J.; Chang, K.-S. Physical, Photochemical, and Extended Piezoelectric Studies of Orthorhombic $ZnSnN_2$ Nanocolumn Arrays. *Appl. Surf. Sci.* **2019**, *470*, 19–26.

(33) Makin, R. A.; York, K.; Durbin, S. M.; Senabulya, N.; Mathis, J.; Clarke, R.; Feldberg, N.; Miska, P.; Jones, C. M.; Deng, Z.; Williams, L.; Kioupakis, E.; Reeves, R. J. Alloy-Free Band Gap Tuning across the Visible Spectrum. *Phys. Rev. Lett.* **2019**, *122* (25), 256403.

(34) Kawamura, F.; Yamada, N.; Cao, X.; Imai, M.; Taniguchi, T. The Bandgap of $ZnSnN_2$ with a Disordered-Wurtzite Structure. *Jpn. J. Appl. Phys.* **2019**, *58* (SC), SC1034.

(35) Chinnakutti, K. kumar; Panneerselvam, V.; Thankaraj Salammal, S. Tailoring Optoelectronic Properties of Earth Abundant $ZnSnN_2$ by Combinatorial RF Magnetron Sputtering. *J. Alloys Compd.* **2019**, *772*, 348–358.

(36) Chinnakutti, K. K.; Panneerselvam, V.; Thankaraj Salammal, S. Investigation on Structural and Optoelectronic Properties of In-Situ Post Growth Annealed $ZnSnN_2$ Thin Films. *Mater. Sci. Semicond. Process.* **2019**, *89*, 234–239.

(37) Cai, X.-M.; Wang, B.; Ye, F.; Vaithinathan, K.; Zeng, J.-J.; Zhang, D.-P.; Fan, P.; Roy, V. A. L. Tuning the Photoluminescence, Conduction Mechanism and Scattering Mechanism of $ZnSnN_2$. *J. Alloys Compd.* **2019**, *779*, 237–243.

(38) Le, D. D.; Ngo, T. S.; Hong, S.-K. Growth of Single Crystal Non-Polar (11 2 ¯ 0) $ZnSnN_2$ Films on Sapphire Substrate. *Appl. Surf. Sci.* **2019**, *481*, 819–824.

(39) Wang, Y.; Ohsawa, T.; Meng, X.; Alnjiman, F.; Pierson, J.-F.; Ohashi, N. Suppressing the Carrier Concentration of Zinc Tin Nitride Thin Films by Excess Zinc Content and Low Temperature Growth. *Appl. Phys. Lett.* **2019**, *115* (23), 232104.

(40) Ye, F.; Chen, Q.-Q.; Cai, X.-M.; Xie, Y.-Z.; Ma, X.-F.; Vaithinathan, K.; Zhang, D.-P.; Fan, P.; Roy, V. A. L. Improving the Chemical Potential of Nitrogen to Tune the Electron Density and Mobility of $ZnSnN_2$. *J. Mater. Chem. C* **2020**, *8* (13), 4314–4320.

(41) Bui, T. N. K.; Halbwax, M.; Vilcot, J.-P. Effect of Sputtering Atmosphere on $ZnSnN_2$ Thin Films Electrical and Optoelectronic Properties. *ECS Trans.* **2020**, *97* (4), 47.

(42) Chinnakutti, K. kumar; Panneerselvam, V.; Thankaraj Salammal, S. Ba-Acceptor Doping in $ZnSnN_2$ by Reactive RF Magnetron Sputtering: (002) Faceted Ba–$ZnSnN_2$ Films. *J. Alloys Compd.* **2021**, *855*, 157380.

(43) Zakutayev, A. Design of Nitride Semiconductors for Solar Energy Conversion. *J. Mater. Chem. A* **2016**, *4* (18), 6742–6754.

(44) Fioretti, A. N.; Stokes, A.; Young, M. R.; Gorman, B.; Toberer, E. S.; Tamboli, A. C.; Zakutayev, A. Effects of Hydrogen on Acceptor Activation in Ternary Nitride Semiconductors. *Adv. Electron. Mater.* **2017**, *3* (3), 1600544.

(45) Wu, X.; Meng, F.; Chu, D.; Yao, M.; Guan, K.; Zhang, D.; Meng, J. Carrier Tuning in $ZnSnN_2$ by Forming Amorphous and Microcrystalline Phases. *Inorg. Chem.* **2019**, *58* (13), 8480–8485.

(46) Pan, J.; Cordell, J.; Tucker, G. J.; Tamboli, A. C.; Zakutayev, A.; Lany, S. Interplay between Composition, Electronic Structure, Disorder, and Doping Due to Dual Sublattice Mixing in Nonequilibrium Synthesis of $ZnSnN_2$:O. *Adv. Mater.* **2019**, *31* (11), 1807406.

(47) Tsunoda, N.; Kumagai, Y.; Takahashi, A.; Oba, F. Electrically Benign Defect Behavior in Zinc Tin Nitride Revealed from First Principles. *Phys. Rev. Appl.* **2018**, *10* (1), 011001.

(48) Bhuiyan, A. G.; Hashimoto, A.; Yamamoto, A. Indium Nitride (InN): A Review on Growth, Characterization, and Properties. *J. Appl. Phys.* **2003**, *94* (5), 2779–2808.

(49) Devia, D. M.; Restrepo-Parra, E.; Arango, P. J.; Tschiptschin, A. P.; Velez, J. M. TiAlN Coatings Deposited by Triode Magnetron Sputtering Varying the Bias Voltage. *Appl. Surf. Sci.* **2011**, *257* (14), 6181–6185.

(50) Tauc, J.; Grigorovici, R.; Vancu, A. Optical Properties and Electronic Structure of Amorphous Germanium. *Phys. Status Solidi B* **1966**, *15* (2), 627–637.

(51) Wang, Z.; Helmersson, U.; Käll, P.-O. Optical Properties of Anatase TiO2 Thin Films Prepared by Aqueous Sol–Gel Process at Low Temperature. *Thin Solid Films* **2002**, *405* (1–2), 50–54.

(52) Charitidis, C.; Patsalas, P.; Logothetidis, S. Optical and Mechanical Performance of Nanostructured Cerium Oxides for Applications in Optical Devices. *J. Phys. Conf. Ser.* **2005**, *10*, 226–229.

(53) Buchholz, D. B.; Liu, J.; Marks, T. J.; Zhang, M.; Chang, R. P. H. Control and Characterization of the Structural, Electrical, and Optical Properties of Amorphous Zinc−Indium−Tin Oxide Thin Films. *ACS Appl. Mater. Interfaces* **2009**, *1* (10), 2147–2153.

(54) Pliatsikas, N.; Siozios, A.; Kassavetis, S.; Vourlias, G.; Patsalas, P. Optical Properties of Nanostructured Al-Rich $Al_{1-x}Ti_xN$ Films. *Surf. Coat. Technol.* **2014**, *257*, 63–69.

(55) Viezbicke, B. D.; Patel, S.; Davis, B. E.; Birnie, D. P. Evaluation of the Tauc Method for Optical Absorption Edge Determination: ZnO Thin Films as a Model System: Tauc Method for Optical Absorption Edge Determination. *Phys. Status Solidi B* **2015**, *252* (8), 1700–1710.

(56) Puspitosari, N.; Longeaud, C. Note: Modification of an FTIR Spectrometer for Optoelectronic Characterizations. *Rev. Sci. Instrum.* **2017**, *88* (8), 086112.

(57) Poruba, A.; Fejfar, A.; Remeš, Z.; Špringer, J.; Vaněček, M.; Kočka, J.; Meier, J.; Torres, P.; Shah, A. Optical Absorption and Light Scattering in Microcrystalline Silicon Thin Films and Solar Cells. *J. Appl. Phys.* **2000**, *88* (1), 148–160.

(58) Kresse, G.; Furthmüller, J. Efficiency of Ab-Initio Total Energy Calculations for Metals and Semiconductors Using a Plane-Wave Basis Set. *Comput. Mater. Sci.* **1996**, *6* (1), 15–50.

(59) Kresse, G.; Furthmüller, J. Efficient Iterative Schemes for *Ab Initio* Total-Energy Calculations Using a Plane-Wave Basis Set. *Phys. Rev. B* **1996**, *54* (16), 11169–11186.

(60) Blaha, P., Schwarz, K., Madsen, G. K., Kvasnicka, D., & Luitz, J. wien2k. An augmented plane wave + local orbitals program for calculating crystal properties. Technische Universität Wien: Wien **2001**; 60.

(61) Tran, F.; Blaha, P. Accurate Band Gaps of Semiconductors and Insulators with a Semilocal Exchange-Correlation Potential. *Phys. Rev. Lett.* **2009**, *102* (22), 226401.

(62) Wan, X. S.; Zhao, S. S.; Yang, Y.; Gong, J.; Sun, C. Effects of Nitrogen Pressure and Pulse Bias Voltage on the Properties of Cr−N Coatings Deposited by Arc Ion Plating. *Surf. Coat. Technol.* **2010**, *204* (11), 1800−1810.

(63) Zamani Meymian, M. R.; Delavari Heravi, A.; Kosari Mehr, A. Influence of Bias Voltage on Optical and Structural Characteristics of Cu3N Films Deposited by Reactive RF Magnetron Sputtering in a Pure Nitrogen Atmosphere. *Mater. Sci. Semicond. Process.* **2020**, *112*, 104995.

(64) Kim, J. H.; Chung, K. W. Microstructure and Properties of Silicon Nitride Thin Films Deposited by Reactive Bias Magnetron Sputtering. *J. Appl. Phys.* **1998**, *83* (11), 5831–5839.

(65) Vaz, F.; Carvalho, P.; Cunha, L.; Rebouta, L.; Moura, C.; Alves, E.; Ramos, A. R.; Cavaleiro, A.; Goudeau, Ph.; Rivière, J. P. Property Change in ZrNxOy Thin Films: Effect of the Oxygen Fraction and Bias Voltage. *Thin Solid Films* **2004**, *469−470*, 11−17.

(66) Ruan, J.-L.; Huang, J.-L.; Chen, J. S.; Lii, D.-F. Effects of Substrate Bias on the Reactive Sputtered Zr−Al−N Diffusion Barrier Films. *Surf. Coat. Technol.* **2005**, *200* (5−6), 1652−1658.

(67) Rizzo, A.; Signore, M. A.; Valerini, D.; Altamura, D.; Cappello, A.; Tapfer, L. A Study of Suppression Effect of Oxygen Contamination by Bias Voltage in Reactively Sputtered ZrN Films. *Surf. Coat. Technol*. **2012**, *206* (10), 2711−2718..

(68) Fioretti, A. N.; Toberer, E. S.; Zakutayev, A.; Tamboli, A. C. Effects of Low Temperature Annealing on the Transport Properties of Zinc Tin Nitride. *2015 IEEE 42nd Photovolt. Spec. Conf. PVSC* **2015**, 1–5.

(69) Senabulya, N.; Feldberg, N.; Makin, Robert. A.; Yang, Y.; Shi, G.; Jones, C. M.; Kioupakis, E.; Mathis, J.; Clarke, R.; Durbin, S. M. Stabilization of Orthorhombic Phase in Single-Crystal $ZnSnN_2$ Films. *AIP Adv*. **2016**, *6* (7), 075019.

(70) Hultman, L. Thermal Stability of Nitride Thin. *Vacuum*, *57*(1), **2000** 1-30.

(71) Sangwal, K; Kucharczyk, W. Relationship between density and refractive index of inorganic solids. *J. Phys. D: Appl. Phys.* **1987**, *20*, 522.

(72) Koffyberg, F. P.; Dwight, K.; Wold, A. Interband Transitions of Semiconducting Oxides determined from Photoelectrolysis spectra. **1979**, *30* (7), 5.

(73) Mott, N. F. Conduction in non-crystalline materials. *Philos. Mag*. **1969**, *19*, 835.

(74) Elliot, S. R. Physics of amorphous materials, Longman Group Ltd, London, New York, **1984**.

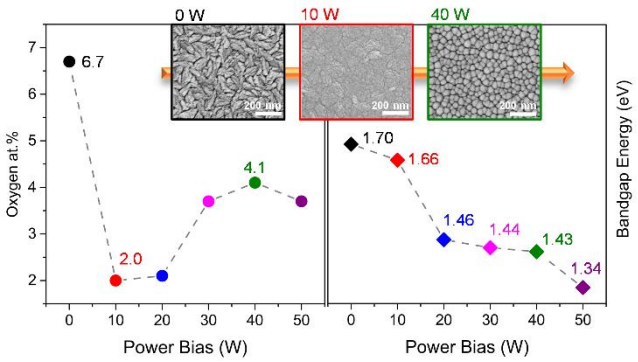
0 W
10 W
40 W
200 nm
200 nm
200 nm
Oxygen at.%
Bandgap Energy (eV)
6.7
2.0
4.1
1.70
1.66
1.46
1.44
1.43
1.34
Power Bias (W)
Power Bias (W)